Hemodynamics in Physio- and Pathological Vessels

4

Shigeru Tada and John M. Tarbell

Abstract

Hemodynamics can be defined as the part of cardiovascular physiology dealing with the forces that drive the blood circulation in mammalian cardiovascular systems. A cardiovascular system is a series of blood vessels connected to the heart. Pressure generated in the heart propels blood through the system continuously. In this chapter, basic hemodynamics essential to interpretation of arterial disease in the aspect of bio-fluid mechanics are introduced. Hemodynamics in bio-fluid mechanics plays an important role in better understanding of clinical and pathological observations and in developing new methods for diagnosis in connection with mathematical models. In particular, hemodynamic factors, such as Wall Shear Stress and Oscillatory Shear Index, correlate substantially with the generation and progression of arterial disease including intimal thickening and atherosclerosis. In the larger vessels, such as the carotid artery, interaction between the vessel wall and the blood flow affects the distribution of hemodynamic factors.

The main scope of this chapter is to introduce hemodynamic applications of mathematical modeling of fluid mechanics. Mathematical models of fluid mechanics are used to quantify the hemodynamic factors and their relationship

S. Tada (✉)
Department of Applied Physics, National Defense Academy, Yokosuka, Kanagawa, Japan
e-mail: stada@nda.ac.jp

J.M. Tarbell
Department of Biomedical Engineering, The City College of New York/CUNY, New York, NY, USA

K. Tanishita, K. Yamamoto (eds.), *Vascular Engineering*,
DOI 10.1007/978-4-431-54801-0_4

to vascular disease. The majority of all cardiovascular diseases and disorders are related to systemic hemodynamic dysfunction. Recent studies of cardiovascular diseases in relation to hemodynamic dysfunction are also briefly reviewed.

Keywords
Hemodynamics • Blood flow • Interstitial flow • Shear stress

4.1 Introduction

In hemodynamic modeling of the cardiovascular system, we can identify three types of cardiovascular subsystems in which mathematical models should be applied differently:

1. Small blood vessels, which include capillaries and arterioles.
   In small blood vessels, non-Newtonian effects are noticeable due to loss of the applicability of the continuum assumption for the dispersed multiphase system of blood. In such vessels, the effect of blood cell aggregation becomes pronounced and exhibits non-Newtonian rheological behaviors, such as the induction of elastic effects associated with the solid-mechanical properties of the red blood cells (RBCs) and their structural formation. Hence non-Newtonian rheological effects should be considered in modeling, simulating, and analyzing the flow of blood in small vessels. The typical example is blood flow in venules with diameter $> \sim 25$ μm. In this scale, the blood flow can be described by a two-phase continuum model; flow in the core is modeled as non-Newtonian, shear-thinning rheological model, or a model for thixotropic fluid that includes time-dependent effects reflecting aggregations/disaggregation kinetics.
2. Large blood vessels, which mainly apply to arteries and veins.
   In large vessels, blood essentially behaves as a Newtonian fluid. Because the blood in a large vessel is normally exposed to a relatively high shear rate and hence the non-Newtonian effects, which are basically induced at low shear rates, are eliminated. Also at this large scale, the blood appears as a homogeneous continuum medium with minor effect of blood cell aggregation. Thus the Navier-Stokes equation for incompressible viscous fluid flow is applicable. However, in some pathological situations such as arterial stenosis, non-Newtonian effects are important even in large vessels. The typical example is blood flow in artery with diameter $>\sim 4$ μm.
3. Porous tissue in the artery wall.
   With the exception of cells at the internal surface of blood vessels, blood does not come into direct contact with the cells it nourishes. For instance, as blood enters the capillaries servicing a tissue space, a large fraction of the plasma, excepting most blood cells, is filtered into the tissue space. The same situation occurs in large artery walls. This is called interstitial fluid. The interstitial fluid brings to cells all of their metabolic requirements and takes away their waste

products. The well-established approach in modeling flow of interstitial fluid in biological tissue is to treat the tissue as a spongy-like porous medium and employ Darcy's law for fluid flow.

4.1.1 Overview of the Chapter

This chapter consists of three sections; Sects. 4.2, 4.3, and 4.4. In the Sect. 4.2, rheological properties of blood, which appear most relevant to slow steady flows in small vessels, are introduced. In the past, the non-Newtonian effects in blood flow originating from the shear rate dependence of the blood viscosity have been extensively studied. A clear correlation has been found between changes in blood viscosity at different shear rates and vascular flow resistance. Thus the rheological properties of steady flow of blood generally have been understood. In this section, basic principles of blood rheology and non-Newtonian effects that alter the characteristics of blood flow are briefly introduced.

In the Sect. 4.3, hemodynamics of large vessels are described. In this subsection, we outline general strategies for modeling blood flow in large arteries. The hemodynamic wall parameters, such as wall shear stress (WSS) and oscillatory shear index (OSI) intended to identify sites where intimal thickening (IT) and thrombosis formation are likely, are also introduced.

Advancing and applying the fundamentals discussed in the early part of Sect. 4.3, the following parts of Sect. 4.3 provide analysis and basic applications of exemplary hemodynamics in the carotid bifurcation. Mathematical models are based on in vivo three-dimensional geometry, pulsatile velocity profiles, and luminal pressure inputs. These data are combined with a linear and isotropic model of the mechanical properties of the carotid artery wall to create fluid-structure interaction (FSI) models of the carotid bifurcation. This model is then used to calculate hemodynamic parameters thought to promote IT and occlusions at the proximal site of the bifurcation.

In the Sect. 4.4, basics of mathematical modeling of interstitial flow in porous media and its application to analysis of the interstitial flow in biological tissues are introduced.

Interstitial fluid flow is the movement of fluid through the extracellular matrix of tissues. This flow provides a necessary mechanism for transporting large proteins through the interstitium and constitutes an important component of the microcirculation. The basic mechanism of mass transfer in artery walls is convection associated with pressure-driven interstitial flow and diffusion caused by concentration gradients. Apart from its role in mass transport, interstitial fluid flow also provides a specific mechanical environment that is important for the physiological activities of interstitial cells. For instance, several in vitro experiments showed that interstitial fluid flow was very important for cell activities and that a flow of μm/s magnitude induced physiological responses from cells.

In the following part of this section, a mathematical model of interstitial fluid flow across an artery wall is introduced. The media of an artery wall is modeled as

an array of smooth muscle cells (SMCs) residing in a matrix comprised of proteoglycan and collagen fibers in the extracellular matrix. As a case study, numerical simulations of interstitial flow emphasizing how the architecture of extracellular matrix affects the WSS on cell membranes is presented to show that interstitial fluid flow imposes significant levels of fluid mechanical force on a cell imbedded in a three-dimensional matrix.

Blood flow plays an important role in guiding the physiological activities of endothelial cells (ECs) and SMCs. However, studies of the effect of interstitial fluid flow on interstitial cells are rare. The case studies are presented in an inductive fashion, i.e. building on simple examples to arrive at more general conclusions.

4.2 Rheological Properties of Blood

4.2.1 Hemodynamic Characteristics of Blood

Blood is a multi-phase mixture of cellular elements suspended in plasma, organic molecules, ions, and dissolved oxygen and carbon dioxide. Plasma is blood from which all cellular elements have been removed and is identical in composition to interstitial fluid except for the presence of some proteins.

The viscosity of blood is determined by several factors such as the hematocrit, viscosity of plasma, and the mechanical properties of blood cells. Hematocrit is the volume percentage of RBC in whole blood (Fig. 4.1). The viscosity of blood, in general, can be described as a function of shear rate and is affected by the applied deformation forces. Thus the blood as a whole behaves essentially as a non-Newtonian fluid showing rheological characteristics; deformation rate dependency of viscosity as well as viscoelasticity, shear thinning, yield stress, and thixotropy although the plasma shows a Newtonian fluid property (Fig. 4.2).

The viscoelastic properties of blood originate from microstructures formed by RBCs. The deformability of the RBCs, cell concentration, and the size of confining vessel are determining factors in the microstructure of RBCs. The typical

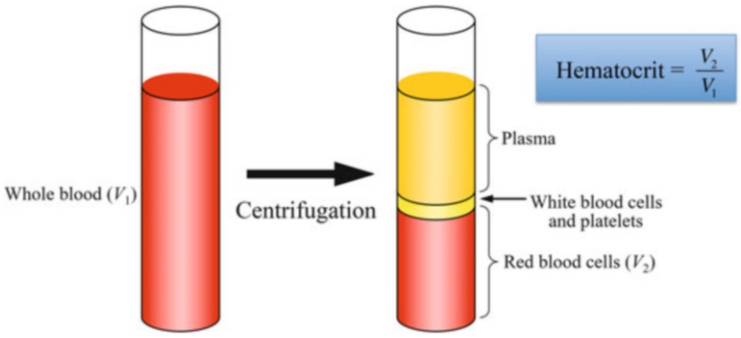

Fig. 4.1 Healthy blood contents and the hematocrit definition

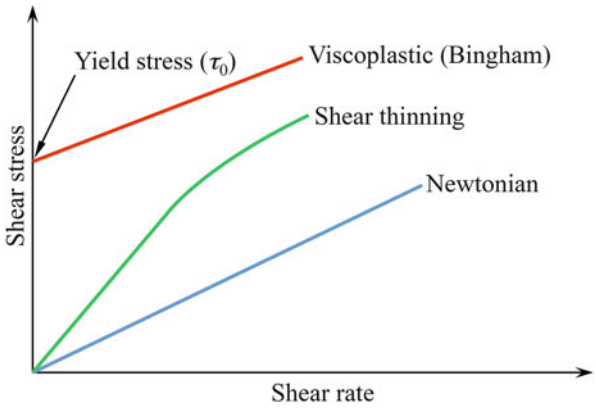

Fig. 4.2 Rheological properties of fluids

microstructure at low shear rate is rouleaux; layers of RBCs adhering face to face like piles of coins to form reversible intercellular contact. Rouleaux formation is highly dependent on the concentration of fibrinogen and globulin in plasma. Note that bovine blood does not form rouleaux because of absence of fibrinogen and globulin in plasma (Fung 1993). The shear thinning nature of blood derives from the tendency of the rouleaux aggregates to disaggregate upon the application of shear.

The source of the yield stress is also the presence of RBCs. Yield stress arises from the aggregation of RBCs at low shear rates to form the microstructures. Under physiological conditions, the RBCs in static or blood flow in a low share rate are likely to adhere to each other to form rouleaux. Therefore, in order to initiate a flow from rest, one needs to have a force large enough to break up the cohesive forces acting among the cells. Previous studies have indicated that yield stress is positively correlated to the concentration of fibrinogen protein in blood plasma and to the hematocrit level (Morris et al. 1989). Yield stress contributes to the blood clotting following injuries and subsequent healing and may also contribute to the formation of thrombi leading to occlusion in some pathological cases such as strokes. Abnormal RBC aggregation has been found to be associated with several diseases and conditions which include diabetics, cardiovascular malfunction, hypertension, and hematological disorders (Ramakrishnan et al. 1999).

The phenomenon of thixotropy results from the microstructure of blood as well. Thixotropy can be explained as a consequence of aggregation of suspended blood cells. If the suspension is at rest, the cell aggregation can form, whereas if the shear stress is added to suspension, the weak physical bonds among cells are broken, and the network among them breaks down into separate aggregates, which can disintegrate further into smaller fragments.

After some time at a given shear rate, a dynamic equilibrium is established between aggregate decomposition and growth, and at higher shear rates, the equilibrium is shifted in the direction of greater dispersion. The relatively long time required for the microstructure to stabilize following a rapid change in the rate of flow makes blood thixotropy.

When blood flows in larger vessels at high shear rates, it behaves like a Newtonian fluid as all of the microstructures are disaggregated, whereas when it flows through small vessels at low shear rates, it shows non-Newtonian behavior. The blood rheology appears most relevant to blood flows with relatively low flow velocities. In this situation, there is cell-free plasma layer adjacent to the vessel wall and core layer of suspension of RBCs. Therefore the blood can't be treated as a single non-Newtonian fluid. Hence, it is appropriate to model blood as a two-fluid model; treating the suspension of RBCs in the core region as a non-Newtonian fluid and the cell-free plasma in the peripheral layer region as Newtonian fluid.

4.2.2 Casson Fluid Model

Among numerous mathematical models of blood rheology proposed in the past, the Casson model has been widely used as the non-Newtonian fluid model to represent the suspension of RBCs in the core region of blood flow in small vessels since the Casson fluid model can predict satisfactorily the flow behavior of a non-Newtonian fluid with yield stress using only a single model parameter. The Casson fluid model could be the best description of blood when it flows through narrow arteries at low shear rates and it can be applied to human blood over a wide range of hematocrits and shear rates.

The mathematical expression of the Casson fluid model is as follows;

$$\sqrt{\tau_{ij}} = \begin{cases} 0 & \text{for } \tau \le \tau_0 \\ \sqrt{\tau_0} + \sqrt{\mu_0}\sqrt{\dot{\gamma}_{ij}} & \text{for } \tau > \tau_0 \end{cases} \tag{4.1}$$

where τ_{ij} is the deviatoric stress tensor (stress tensor of force field per unit area as a result of the resistance to the rate of deformation of fluid element), τ_0 is the yield stress, μ_0 is the viscosity of the Casson fluid above the yield stress, and $\dot{\gamma}_{ij}$ is shear rate.

As a simple application of the Casson fluid model for the hemodynamic analysis of blood flow, let us consider steady blood flow through a small straight vessel.

As shown in Fig. 4.3, the volumetric flow rate of a Casson fluid, Q, through a small straight vessel of radius R and length L_v is given as

$$Q = \frac{\pi R^4}{8\mu_0}\left(\frac{\Delta p}{L_v}\right)\left(1 - \frac{16}{7}\sqrt{\kappa} + \frac{4}{3}\kappa - \frac{1}{21}\kappa^4\right) \tag{4.2}$$

where Δp is the pressure difference across the whole length of the vessel and κ is the non-dimensional yield stress described as

$$\kappa = \frac{2L_v\tau_0}{\Delta p R} \tag{4.3}$$

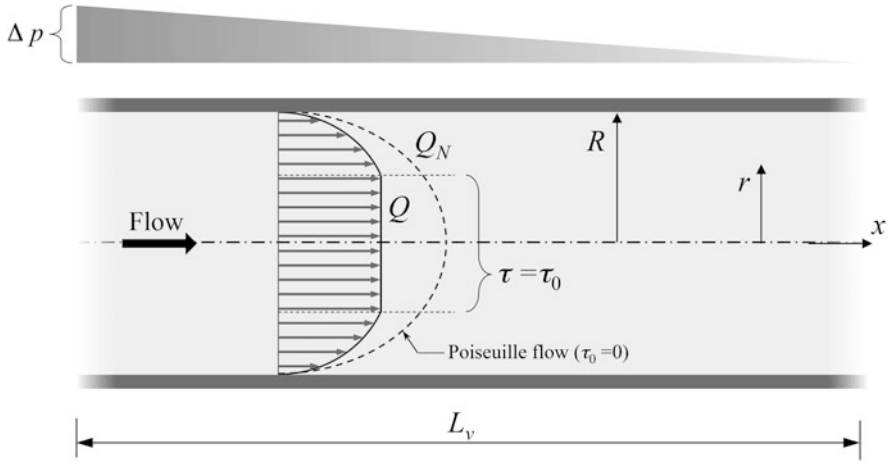

Fig. 4.3 Steady flow of the Casson fluid in a straight circular tube of radius R and length L_v

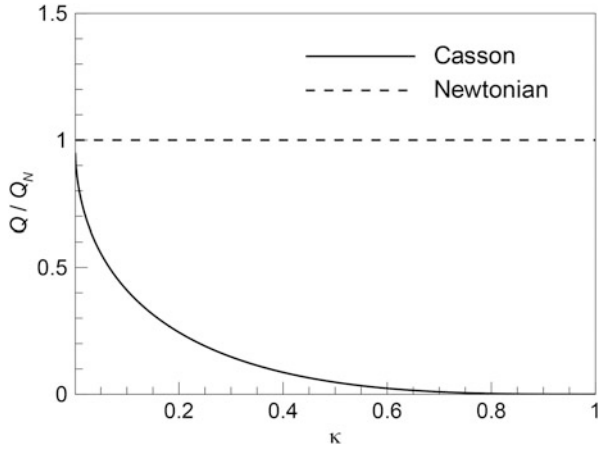

Fig. 4.4 Relationship between the volumetric flow rate of the Casson fluid, Q/Q_N, and the non-dimensional yield stress, κ. The volumetric flow of the Casson fluid is normalized to that of the Newtonian fluid, Q_N

In this model, when κ approaches 0 this model approaches the Newtonian fluid model. The relationship between the volumetric flow rate of the Casson fluid and the non-dimensional yield stress is shown in Fig. 4.4. In the figure, the volumetric flow of the Casson fluid is normalized to that of the Newtonian fluid

$$Q_N = \frac{\pi R^4}{8\mu_0}\left(\frac{\Delta p}{L_v}\right) \tag{4.4}$$

as Q/Q_N. Equation (4.4) is the well-known Hagen-Poiseuille solution. For steady blood flow, the non-Newtonian nature of blood acts as a factor to increase the resistance. An interesting feature is that the ratio of volumetric flow, Q/Q_N, decreases as the size of vessel radius increases since the non-dimensional parameter, κ, decreases with the increase in the radius of vessel, R in Eq. (4.2). In other words, the non-Newtonian nature of blood acts as a regulating factor to reduce the hydraulic resistance in larger vessels, and hence contributes to the body protection.

4.2.3 Alternations of Blood Rheology in Pathological Conditions

The rheological characteristics of blood continue to be of great interest in circulatory physiology with numerous publications dealing with topics such as blood and plasma viscosity, blood cell aggregation, and deformability. In particular, increased blood viscosity, impaired RBC deformability, and increased RBC aggregation are reported in a variety of cardiovascular diseases (Chien et al. 1987). It has been shown that in patients with myocardial ischemia and diabetes mellitus, disorders of blood rheology and endothelial dysfunction develop (Shul'man et al. 2006).

Ischemic diseases of various organs are known to be associated with the impairment of blood rheology (Kesmarky et al. 1998). Hypertension is also characterized by alterations of blood rheology. Hypertension is a complex pathphysiological process (Ajmani 1997). Especially the advanced forms of hypertension are associated with vascular damage, and this damage is claimed to be the cause of alterations of blood rheology. Recent evidence suggests that altered RBC rheological properties might be the underlying cause of some types of hypertension. RBC aggregation was found to be increased significantly in the hypertensive rats (Bor-Kucukkatay et al. 2000).

Diabetes mellitus is a disease process that is accompanied by microcirculatory disturbances. Diabetes mellitus is characterized by abnormal carbohydrate metabolism arising from insulin deficiency. Insulin is the key hormone in blood glucose homeostasis. The consequent elevation of glucose in the blood plasma affects RBCs and vascular ECs, including the walls of capillaries. Rheological changes such as augmented aggregation of RBC, decreased deformability of RBC, and increased viscosity of blood and plasma lead to disturbances of microcirculation in the terminal vascular system. A number of studies have reported increased blood and plasma viscosity, enhanced RBC aggregation, and altered RBC deformability in diabetes mellitus (McMillan 1993).

4.3 Hemodynamics of Large Vessels

4.3.1 Characteristics of Blood Flow in Large Vessels

In large vessels, the blood essentially behaves as a Newtonian fluid. The blood in large vessels is normally exposed to a relatively high shear rates, and therefore the non-Newtonian effects exhibited at low shear play a minor role. Also at this scale the blood appears as a homogeneous continuum medium with diminishing effect of blood cell aggregation because the vessel diameters are large compared with the individual cell diameters. However, in some pathological situations such as the severe stenosis where the rapid change in the shear magnitude occurs, non-Newtonian effects are important even in the large vessels and therefore they should be taken into consideration in the hemodynamic analysis.

In previous studies of hemodynamics in large vessels, the non-Newtonian phenomena in the blood have not been given sufficient attention for the reasons mentioned above. In the analysis of hemodynamic in large vessels, blood is generally assumed Newtonian, and non-Newtonian effects are ignored for simplification of the flow models and their computational implementation. When the shear rate is high, the blood viscosity is independent of shear rate. With a reduction of shear rate, the blood viscosity increases moderately until a shear rate less than ~100 1/s, where it rises extremely steeply. This behavior of blood viscosity can be well predicted by the use of the Casson fluid model. For instance, from the Casson fluid model Eq. (4.1) and general form of the constitutive equation of steady non-Newtonian fluid flow

$$\tau_{ij} = \mu(\dot{\gamma})\dot{\gamma} \tag{4.5}$$

one can obtain the following expression for the Casson viscosity as a function of the shear rate (Kleinstreuer 2006);

$$\mu(\dot{\gamma}) = \frac{1}{\dot{\gamma}}\left[C_1(Ht) + C_2(Ht)\sqrt{\dot{\gamma}}\right]^2 \tag{4.6}$$

where Ht is the hematocrit. The coefficients $C_1(Ht)$ and $C_2(Ht)$ in Eq. (4.6) were determined for $Ht = 40\%$ as $C_1(40) = 0.2$ $(\text{dyn/cm}^2)^{1/2}$ and $C_2(40) = 0.18$ $(\text{dyn/cm}^2)^{1/2}$, based on Merrill's experimental data (1969). Figure 4.5 shows the relationship between the shear rate and apparent viscosity of the Casson fluid exposed to simple shear flow. The graph implies that the Casson viscosity, Eq. (4.6), approaches the Newtonian viscosity as the shear rate increases. The shear rate range for which non-Newtonian effects are considered significant is lower than ~100 l/s. The blood is generally treated as a Newtonian fluid above this limit, which is realized at the blood flow ranges in large and medium size vessels with the diameter of about >1000 μm. In other words, Casson fluid model is adequate for the representation of the simple shear behavior of blood in vessels with the diameter of 130–1000 μm.

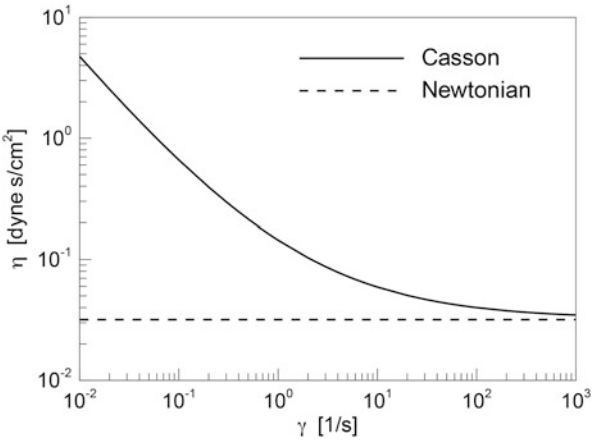

Fig. 4.5 The relationship between the shear rate, γ, and the apparent viscosity of the Casson fluid, η, exposed to a simple shear flow

In the previous sections, deformability of vessel walls has not been mentioned. However, it has been well known that vessel walls undergo mild distention with respect to the original dimensions. The rigid-wall approximation for the artery wall is justified by the observation that, under normal conditions, wall deformability does not significantly alter the velocity field. This approximation may not be valid for large and medium size vessels where wall deformations are not negligible. In such situations, large deformation theory can be applied to model artery wall deformation. It is reasonable to take the effects of wall distension on the flow field in describing hemodynamics of large and medium size vessels.

4.3.2 Mathematical Formulation of Blood Flow in Large Vessels

4.3.2.1 Blood Flow Modeling

The approximation of blood as a Newtonian fluid is an acceptable assumption and not far from reality for many circumstances such as the flow in large and medium size vessels at medium and high shear rates under non-pathological conditions. Consequently blood can be considered as a homogeneous, incompressible Newtonian fluid. Under these assumptions, the hemodynamics problem is expressed by the conservation of the two physical properties of mass and momentum, giving rise to the following set of equations:

$$\begin{cases} \dfrac{\partial u_j}{\partial x_j} = 0 \\ \dfrac{\partial u_i}{\partial t} + u_j \dfrac{\partial u_i}{\partial x_j} = -\dfrac{1}{\rho}\dfrac{\partial p}{\partial x_i} + \dfrac{\partial \tau_{ij}}{\partial x_j} \end{cases} \tag{4.7}$$

where the first equation describes the law of mass conservation and the second equation describes the law of momentum conservation. In Eq. (4.7), u_i represents

velocity, while p and τ_{ij} are pressure and viscous stress tensors respectively, which are the isotropic and deviatoric parts of the stress tensor σ_{ij}:

$$\sigma_{ij} = -p\delta_{ij} + \tau_{ij} \tag{4.8}$$

For an incompressible Newtonian fluid, the constitutive relation between τ_{ij} and the rate of strain tensor e_{ij} is described as

$$\tau_{ij} = 2\mu e_{ij} \tag{4.9}$$

where μ is viscosity of a Newtonian fluid. Substituting Eq. (4.9) into the momentum conservation equation yields the Navier-Stokes equation:

$$\frac{\partial u_i}{\partial t} + u_j \frac{\partial u_i}{\partial x_j} = -\frac{1}{\rho}\frac{\partial p}{\partial x_i} + \nu \frac{\partial u_i}{\partial x_j \partial x_j} \tag{4.10}$$

4.3.2.2 Wall Motion Modeling

In the physiological range of blood pressure, the stress-strain relationship of the artery wall may be considered as linear during the pressure pulse. Large deformation theory is used to model artery wall deformation. For simple approximation, the artery can be modeled as a thick-walled linearly elastic circular cylindrical tube consisting of a homogeneous material. The equations governing the movement of the elastic wall are the momentum equations, the equilibrium conditions, and the constitutive equations, respectively:

$$\rho \frac{\partial^2}{\partial t^2} d_i = \frac{\partial}{\partial x_j}\sigma_{ij} + \rho f_i \tag{4.11}$$

$$\sigma_{ij} n_j = {}^{s}t_i \tag{4.12}$$

$$\sigma_{ij} = D_{ijkl}\,\varepsilon_{kl} \tag{4.13}$$

where $\partial^2 d_i / \partial t^2$ represents the acceleration of a material point (where displacement is defined as $d_i = x_i - x_{i0}$, and x_{i0} is the stress-free position) at time t, n_j is the outward pointing normal vector on the structural boundary at time t, ${}^{s}t_i$ is the surface traction vector at time t, D_{ijkl} is the material elasticity tensor, and ε_{ij} is the infinitesimal strain tensor.

4.3.3 Hemodynamic Wall Parameters

It has been well known that EC injury or dysfunction and the interaction of blood cells with the vascular surface play significant roles in the evolution of IT and atherosclerosis development. Hemodynamic wall parameters are intended to

identify sites where IT and thrombosis formation are likely based on hemodynamic wall interactions. In other words, identifying sites of EC dysfunction has been a primary purpose of the wall parameters of WSS-based hemodynamics. In the following, some basic wall parameters are introduced.

4.3.3.1 Wall Shear Stress (WSS)

The shear stress is a tensor within the flow field and reduces to a vector on a solid surface:

$$\tau_w = n \bullet \tau \tag{4.14}$$

where n is the local surface normal vector. The magnitude of the time average WSS vector can be written as

$$\mathrm{WSS} = \overline{\tau}_w = \left| \frac{1}{T} \int_0^T \tau_w \, dt \right| \tag{4.15}$$

Alternatively, the time average of the WSS magnitude can be written

$$|\overline{\tau}_w| = \frac{1}{T} \int_0^T |\tau_w| \, dt \tag{4.16}$$

4.3.3.2 Oscillatory Shear Index (OSI)

Cyclic departure of the WSS vector from its predominant axial alignment indicates flow disruption over time and is known as the oscillatory shear index, or OSI (Ku et al. 1985). The OSI, therefore, quantifies disturbed flow interaction with the wall and is formulated as

$$\mathrm{OSI} = \frac{1}{2} \left(1 - \frac{\overline{\tau}_w}{|\overline{\tau}_w|} \right) \tag{4.17}$$

where $\overline{\tau}_w$ is the instantaneous WSS vector. The OSI can vary from 0 to 0.5, indicating the least and most severe temporal shear rate conditions, respectively.

4.3.3.3 Stress Phase Angle (SPA)

The WSS of flowing blood and the circumferential strain (CS) induced by hoop stresses that balance blood pressure are imposed on ECs. These mechanical forces are known to influence gene expression and protein and metabolite secretion of EC and are believed to play a role in the localization of atherosclerosis in regions of curvature and branching in arteries (Chien 2003). Previous studies have provided evidence that the temporal phase angle between CS and WSS, the stress phase angle (SPA), is most negative (mechanical forces are most out-of-phase) in precisely those regions where atherosclerotic plaques are localized (Thomas et al. 2002).

4.3.4 Hemodynamic Analysis of Flow in Carotid Bifurcation (Tada and Tarbell 2005)

From the physiological point of view, blood is a shear-rate dependent fluid flowing in pulsatile fashion through non-rigid bifurcating tubes with variable cross sections. While pulsatile flow of an incompressible Newtonian fluid in a bifurcation with a slightly elastic tube is a reasonable starting point when modeling the hemodynamics in actual arterial trees. A carotid bifurcation, as considered here, is the primary application site for most researchers. In modeling the hemodynamics of the carotid bifurcation, inlet and boundary conditions, in addition to the no-slip wall condition, were selected in a manner to: (a) match physiological conditions as closely as possible with available data and (b) facilitate numerical simulation.

4.3.4.1 Model Geometry, the Solution Method, and the Computational Results

The model geometry is shown in Fig. 4.6, and representative dimensions are listed in Table 4.1. For the inlet boundary conditions, a uniform pressure varying with time was applied. The waveform of the common carotid artery (CCA) wall distention was assumed to be that of the inlet pressure. Values of 110 and 76 mmHg were used for the peak systolic and minimum of diastolic pressures, respectively. For the outlet boundary conditions of the internal carotid artery (ICA) and external carotid artery (ECA), waveforms of flow obtained from phase-contrast MRI velocity measurements were used. A fully developed parabolic velocity profile was applied at the downstream end of both the ICA and ECA. For the modeling of elastic wall, an incompressible (Poisson's ratio = 0.5) linear elastic model having a Young's modulus of 5.0×10^6 dyn/cm^2 was applied. Moreover, rigid and fixed cylindrical segments of length $2.0a$ (a: the internal diameter of CCA) were applied to support the elastic bifurcation tube at the upstream end of the CCA and the downstream end of both the ICA and ECA. The artery wall was assumed to be a solid wall impermeable to blood plasma. The blood was assumed to be Newtonian with a density of 1.05 g/cm^3 and a viscosity of 3.5×10^{-2} dyn s/cm^2.

Fluid and solid equations Eqs. (4.10, 4.11, 4.12, and 4.13) together with coupling conditions were solved by the Arbitrary Lagrangian Eulerian (ALE) based loose coupling algorithm using FIDAP 8.72 (FLUENT) software. A gradually finer mesh toward the solid surface was taken in the grid system of the fluid phase to ensure enough spatial resolution in the boundary layer of the flow field to evaluate WSS accurately as shown in Fig. 4.6. The element numbers for the fluid and wall models were 60,000 and 36,000, respectively. The governing equations for both the fluid and solid were transformed into algebraic equations using the finite element method. The resulting algebraic equations were solved by the direct Gaussian elimination method.

Figure 4.7 shows the instantaneous streamlines of flow colored according to the flow velocity at the time of peak systole (a) and end diastole (b). The times of peak systole and end diastole are presented as dotted lines in the inset graphs showing the flow rates vs. time (t) for one cardiac time period (T). The starting points (seeds) of the streamlines in the cross-section of the CCA entrance were given as shown in the right-hand-side of panel (b). The cross-sectional velocity profiles at the CCA

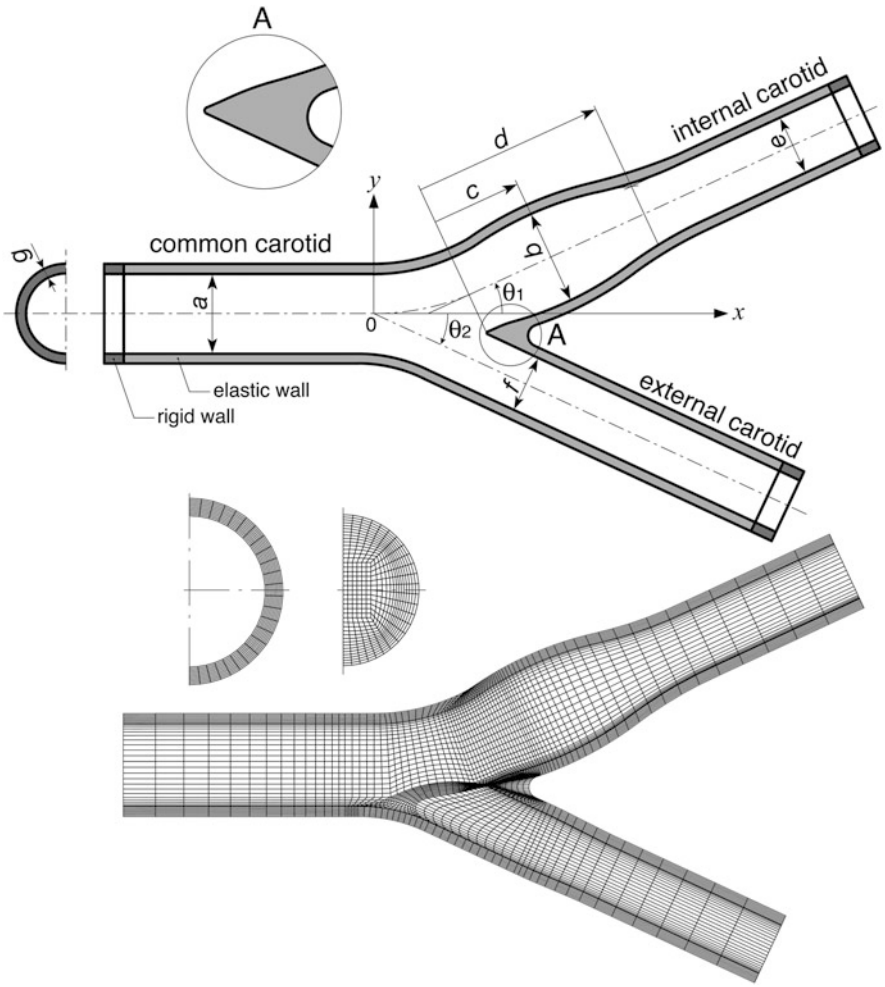

Fig. 4.6 (*Top*) Three-dimensional model geometry of the carotid bifurcation. (*Bottom*) The structured grid system consists of a grid system for the fluid phase and a grid system for the solid phase (Reproduced from Tada and Tarbell 2005 with permission from Springer)

Table 4.1 Representative values of bifurcation geometry

Location in Fig. 4.6	Labels	× a ($a = 0.6$ cm)
CCA internal diameter	a	1.000
Max. sinus internal diameter	b	1.110
	c	0.910
	d	2.300
ICA internal diameter	e	0.740
ECA internal diameter	f	0.650
Thickness of artery wall	g	0.117
ICA bifurcation angle	θ_1	25.0 °
ECA bifurcation angle	θ_2	25.0 °

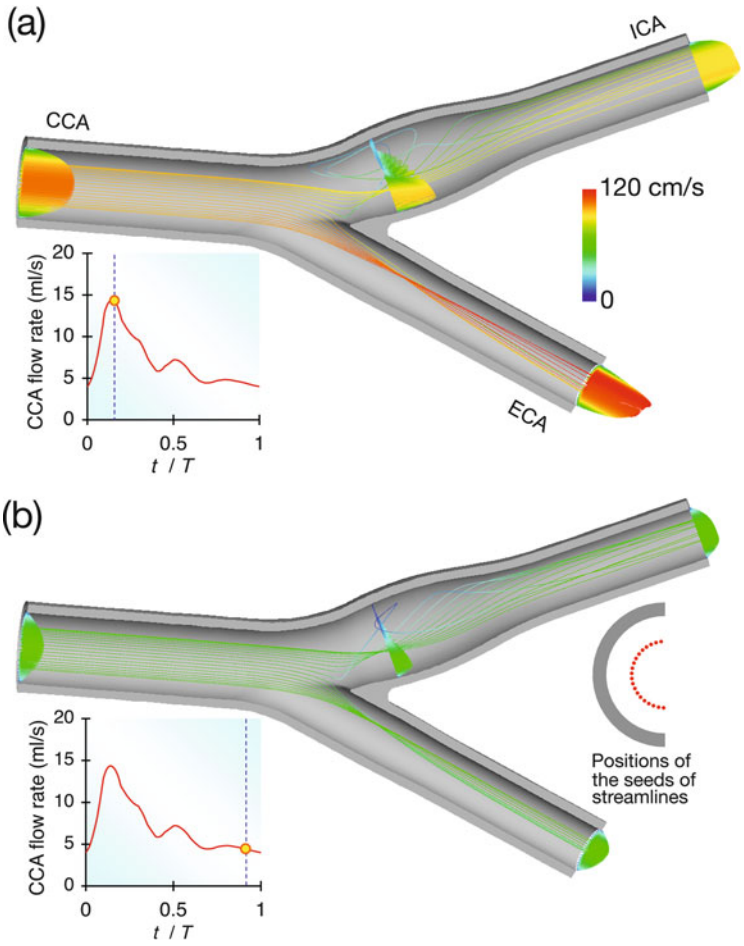

Fig. 4.7 Instantaneous streamlines colored according to the flow velocity are shown at the times of (**a**) peak systole and (**b**) end diastole. The starting points of the streamlines over the CCA entrance cross-section are distributed as presented in the right-hand side of panel (**b**). The velocity profiles at the CCA entrance, at the ICA and ECA exits, and in the middle of the ICA sinus are also depicted

entrance, at the exits of both ICA and ECA, and at the middle of the ICA sinus, are also shown. The flow pattern in the ICA sinus at the time of peak systole is complex because of flow separation, reversal, and swirling caused by the strong secondary flow. The flow divider generates vortices along the inside wall of the ICA sinus, although flow reversal is generated along the outside wall at the sinus. The size and position of the recirculation zone change only slightly during a single cardiac cycle. However, the flow velocity in the ICA sinus changes considerably with time. The flow velocity near the wall in the recirculation zone is very low for most of the time period of one cardiac cycle, except at the time of peak systole as shown in (b)

In Fig. 4.8, the distribution of the mean WSS, OSI, and SPA over the internal surface of the wall were displayed for comparison. The SPA is the phase angle

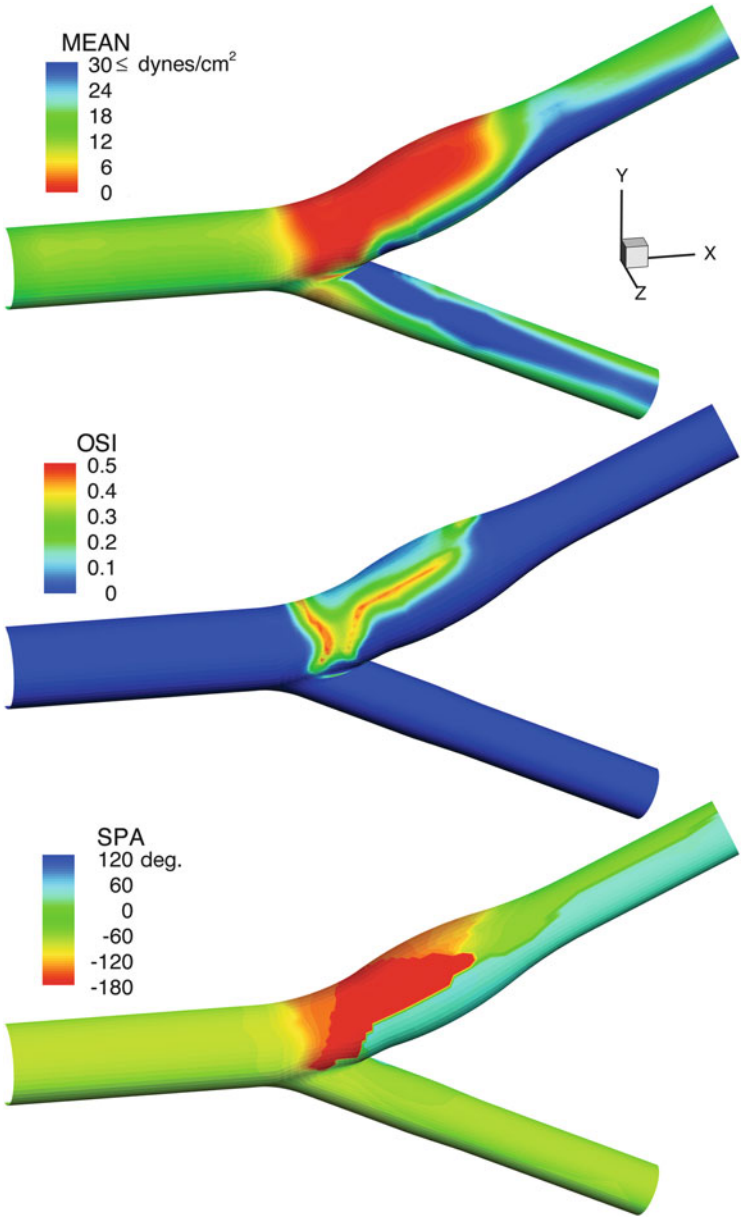

Fig. 4.8 Color contour-plots of time-average wall shear stress (mean WSS [dyn/cm^2]), oscillatory shear index (OSI, dimensionless), and stress phase angle of the first harmonic (SPA [deg.]) over the cardiac cycle (Reproduced from Tada and Tarbell 2005 with permission from Springer)

between the first harmonic components of the CS and WSS waves. The zone of high negative SPA ($< -90°$) at the sinus (bottom) is well correlated with the low mean WSS (top) and high OSI (middle) domains. The low WSS region appears at the ICA outer wall in the sinus region and is a common feature of the WSS distribution in the carotid sinus regardless of the detailed geometric features of the bifurcation and flow waveforms.

4.3.5 Arterial Disease Formation and Hemodynamic Factors

One of the major consequences of carotid artery disease is stenosis. Carotid artery stenosis occurs when the carotid arteries become narrowed. The narrowing of the carotid arteries is most commonly related to atherosclerosis. Atherosclerosis is generally characterized by the accumulation of fatty deposits right beneath the innermost endothelial linings: leading to complex cellular reactions and the formation of IT (Kohler et al. 1992). IT forms non-randomly at locations in bends and bifurcations, where the local flow can be classified as 'disturbed flow' and is associated with low WSS and oscillatory or reciprocating flow. Numerous in vitro studies have indicated that low WSS may contribute to IT and development of atherosclerosis.

If the disease process progresses, plaque formation may take place. Plaque is made up of SMCs, monocyte macrophages, foam cells, and cholesterol. The growth of plaque narrows the luminal space of arteries and can decrease blood flow or completely block the flow of blood to the brain. The interested reader is referred to Tarbell et al. (2014) for the details of the recent advances in pathological hemodynamics.

4.4 Interstitial Flow in Arterial Tissues

Interstitial flow plays important roles in the pathogenesis in arterial tissues. To investigate these roles, a comprehensive consideration of the flow in the interstitial space and how it affects such processes is critical.

As shown in Fig. 4.9, a typical mammalian artery consists of the following four structurally distinct regions: endothelium, intima, media, and adventitia. The endothelium is the innermost thin layer of arterial tissue consists of a single layer of ECs. The endothelium not only provides a structural barrier between the circulation and surrounding tissue, but ECs also secrete mediators that influence vascular hemodynamics in the physiologic state, such as nitric oxide (NO), prostacyclin (PGI_2), platelet-activating factor (PAF), and endothelin-1 (ET-1). The intima is a thin layer of basement matrix, separated from the media by the internal elastic lamina (IEL), which is a fenestrated layer of elastic tissue. The media is viewed as a porous heterogeneous medium consisting of a continuous extracellular matrix phase with embedded SMCs. The adventitia is the outermost layer of the artery wall typically

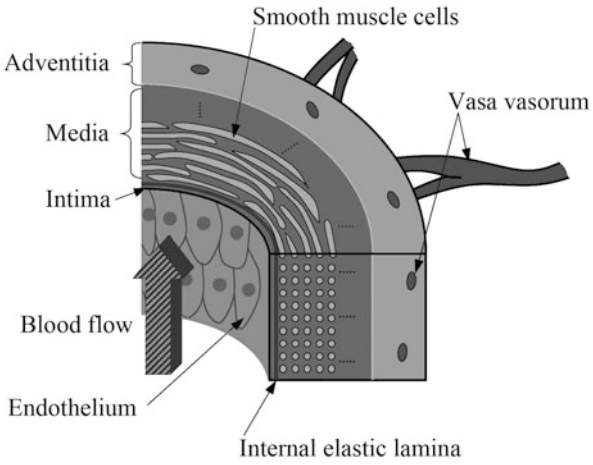

Fig. 4.9 Transverse sectional view of a blood vessel wall. The bulk of the blood vessel wall consists of the media and adventitia. There are some capillaries (vasa vasorum) in adventitia. The innermost layer of vessel wall (intima) is a single layer of endothelial cells (ECs) and a thin layer of basement matrix. The internal elastic lamina (IEL), an impermeable barrier to water flow except for fenestral pores, separates the intima from media. Between smooth muscle cells (SMCs) in the media is an interstitial phase containing proteoglycan and collagen fibers (Reproduced from Tada and Ozono 2011 with permission from Springer)

comprised of loose connective tissue and fibroblasts. There are some capillaries (e.g., vasa vasorum) in the adventitia.

Interstitial fluid that has gained entry to the intima by crossing the endothelium passes through the fenestrae in the IEL and enters the media toward the adventitia and embedded SMCs. It is well known that WSS associated with blood flow can affect EC biology and may play an important role in arterial disease. For instance, WSS on ECs can stimulate the release of Nitrogen Oxide (NO) that causes smooth muscle relaxation. This represents an indirect effect of flow on SMCs. SMCs are also exposed directly to interstitial flow.

Here we introduce a mathematical model of interstitial flow in arterial tissue that describes the hemodynamics of the interstitial flow in arterial tissues. The importance of hemodynamic factors on cell biology will be discussed in the following sections.

4.4.1 Mathematical Formulation of the Flow in Porous Media

Most of arterial tissue, e.g. intima and media, are biphasic materials, comprised mainly of water enclosed within an elastic matrix of elastin and collagen fibers. These layers can be approximated as isotropic porous media layers with different

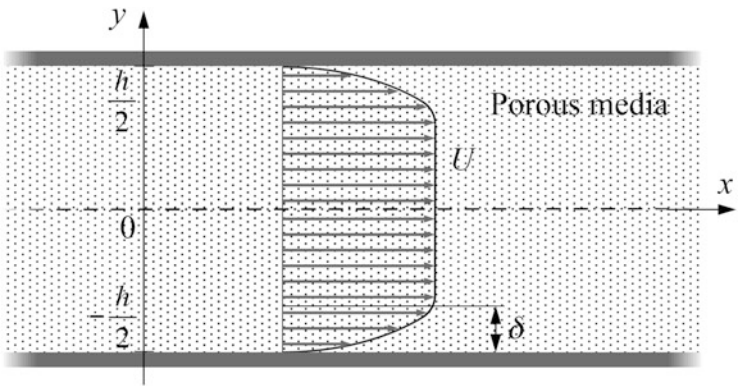

Fig. 4.10 A Newtonian fluid flow in a parallel-plate channel filled with a homogeneous porous medium. The channel with the separation distance h was aligned with the x-axis. The flow was assumed to be steady and axisymmetric about the center axis of the channel

values of permeability to fluid. The flow of interstitial fluid through a porous media is described by Darcy's Law:

$$\nabla P = -\frac{\mu}{K_p} U \tag{4.18}$$

where P is the pressure, U is the averaged (macroscopic) velocity, μ is the viscosity of interstitial fluid, K_p is the hydraulic permeability of the porous media, which has dimension of (length)^2 and depends on the geometry of the porous media. Although this model has been utilized successfully in several biomedical applications such as blood perfusion through soft tissues, it is not valid when the boundaries of the porous media should be taken into account. Because Darcy's model ignores the boundary effects on the flow, the Brinkman model is usually employed:

$$\nabla P = -\frac{\mu}{K_p} U + \mu \nabla^2 U \tag{4.19}$$

The second term on the right-hand side of Eq. (4.19) represents the viscous force which is required to satisfy a no-slip boundary condition on the solid surface.

The most general case in which the viscous force plays an important role is for flow over a plane solid surface as illustrated in Fig. 4.10. The equation governing a fully developed flow in a two-dimensional porous channel bounded by planar solid walls as shown in Fig. 4.10 is given by:

$$\frac{\partial P}{\partial x} = -\frac{\mu}{K_p} U + \mu \frac{\partial^2 U}{\partial y^2} \tag{4.20}$$

with the boundary conditions:

$$U|_{y=-h/2} = 0, \qquad \left.\frac{\partial U}{\partial y}\right|_{y=0} = 0 \tag{4.21}$$

The solution of Eqs. (4.20 and 4.21) becomes:

$$U = \frac{K_p}{\mu}\left(-\frac{\partial P}{\partial x}\right)\left[1 - \frac{\cos\ h\frac{y}{\sqrt{K_p}}}{\cos\ h\frac{h}{2\sqrt{K_p}}}\right] \tag{4.22}$$

The velocity distribution, Eq. (4.22), can be rewritten with the use of the mean interstitial flow velocity:

$$U_m = \frac{1}{d}\int_{-2/h}^{2/h} U dy \tag{4.23}$$

By introducing non-dimensional velocity, non-dimensional channel width, and a non-dimensional parameter, the Darcy number:

$$U^* = \frac{U}{U_m}, \qquad y^* = \frac{y}{h/2}, \qquad Da = \frac{2K_p}{h^2} \tag{4.24}$$

the non-dimensional form of the flow velocity:

$$U^* = \frac{1}{1 - \sqrt{Da}\ \tan\ h\frac{1}{\sqrt{Da}}}\left(\frac{1 - \cos\ h\frac{y^*}{\sqrt{Da}}}{\cos\ h\frac{1}{\sqrt{Da}}}\right) \tag{4.25}$$

can be obtained.

The velocity distribution across the channel width is shown as a function of Darcy number, Da, in Fig. 4.11. The shape of the flow distribution becomes parabolic for greater Da, namely the Hagen-Poiseuille solution:

$$\lim_{Da\to\infty} U^* = \frac{3}{2}\left(1 - y^{*^2}\right), \tag{4.26}$$

while it becomes rectangular with very thin boundary layer at the wall surface for smaller value of Da:

$$\lim_{Da\to 0} U^* = 1. \tag{4.27}$$

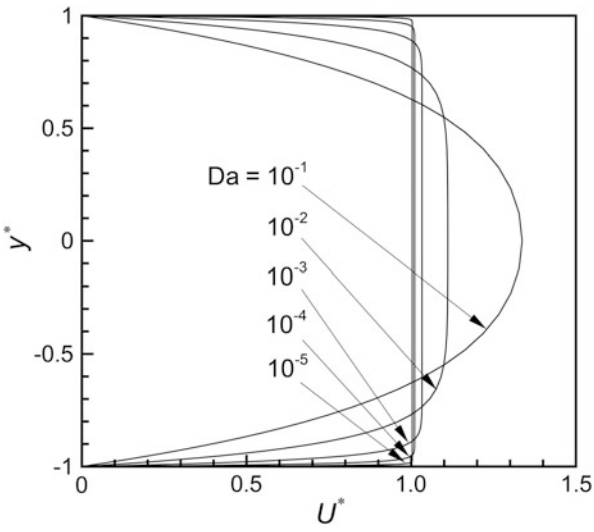

Fig. 4.11 Variations of velocity distribution of steady flow in porous channel with the Darcy number, Da. Values are normalized to the average flow velocity

The thickness of boundary layer of the interstitial flow, δ, can be roughly estimated by the dimensional analysis of the governing Eq. (4.20):

$$\frac{\partial P}{\partial x} = \underbrace{-\frac{\mu}{K_p}U}_{1/K_p} + \underbrace{\mu\frac{\partial^2 U}{\partial y^2}}_{1/\delta^2} \tag{4.28}$$

The first term in the right-hand-side of Eq. (4.28) has the order of magnitude, $\mu U/K_p$, while the second term has order of magnitude $\mu U/\delta^2$. These two terms should have comparable orders of magnitude. Hence, the order of the boundary layer thickness, δ, can be estimated as a function of the hydraulic permeability of porous media, K_p:

$$\delta \sim \sqrt{K_p} \tag{4.29}$$

Therefore, the order of magnitude of WSS at the wall surface can be estimated in a similar way:

$$\tau_w \sim \mu\frac{U}{\sqrt{K_p}} \tag{4.30}$$

The WSS of the interstitial flow can take on extremely large values even though the interstitial flow velocity is very low. For instance, the viscosity of interstitial fluid (water) is on the order of 10^{-3} Pa s, the hydraulic permeability of the tissue is on the order of 10^{-14} cm^2, the velocity of the interstitial flow is on the order of 10^{-6} cm/s.

By accounting for these values, the WSS, Eq. (4.30), is found to be on the order of 0.1 dyn/cm^2, which is in the range known to affect the biology of ECs exposed to blood flow.

4.4.2 Modeling of Interstitial Flow in Artery Wall

4.4.2.1 Analytical Solution for the Flow in the Media

In the following, a mathematical model of the interstitial flow in the media is introduced for a case study. The present model is certainly an idealization of the true architecture of the media of the artery wall (Clark and Glagov 1985).

The media, depicted in Fig. 4.12, is modeled as a periodic square array of cylindrical SMCs residing in a matrix comprised of proteoglycan and collagen fibers. The cells are treated as impermeable obstacles to flow due to the cell membrane's low hydraulic conductance, which is typically two orders of magnitude lower than the conductance of the interstitium (Levick 1987). The flow is assumed to be perpendicular to the longitudinal axis of the cylindrical SMCs. Namely the corresponding flow field can be treated as a two-dimensional flow problem.

The non-dimensional governing equations for the flow field are the Brinkman equation and the law of mass conservation:

$$\begin{aligned} \nabla p &= -\boldsymbol{u} + \frac{1}{\alpha^2}\nabla^2 \boldsymbol{u} \\ \nabla \bullet \boldsymbol{u} &= 0 \end{aligned} \tag{4.31}$$

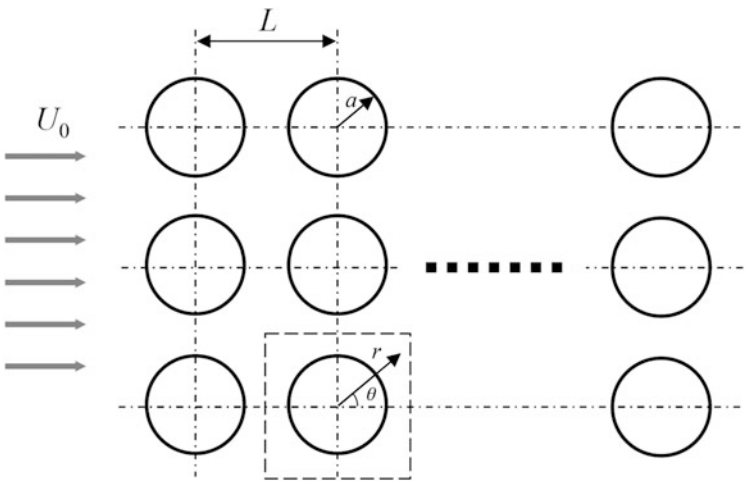

Fig. 4.12 Schematic illustration of the analysis model; a periodic square array of cylindrical SMCs residing in a matrix comprised of proteoglycan and collagen fibers

where p and u are the non-dimensional pressure and velocity, $p = K_p P/a\mu U_0$, $\boldsymbol{u} = U/U_0$, and a is the radius of SMC, U_0 is the representative flow velocity, $\alpha = a^2/K_p$. The solution of Eq. (4.31) must satisfy a no-slip boundary condition on the SMC surface. The velocity field outside the boundary layer is determined by solving the outer flow defined by the Darcy equation, and the velocity field inside the boundary layer is determined by the first equation of Eq. (4.31), the Brinkman equation. These two velocity fields must match at the edge of the boundary layer. The asymptotic solutions for $\alpha \gg 1$ can be obtained in the form of a sum of infinite power series of radial and circumferential coordinate variables (Wang and Tarbell 1995):

$$p = \sum_{n=0}^{\infty} A_n \left[r^{2n+1} + \left(\frac{1}{r}\right)^{2n+1} \right] \cos\,(2n+1)\,\theta \tag{4.32}$$

$$u_r = -\sum_{n=0}^{\infty} (2n+1)\,A_n \left[r^{2n} - \left(\frac{1}{r}\right)^{2n+2} \right] \cos\,(2n+1)\,\theta \tag{4.33}$$

$$u_\theta = \sum_{n=0}^{\infty} (2n+1)\,A_n \left[r^{2n} + \left(\frac{1}{r}\right)^{2n+2} - 2e^{-\eta} \right] \sin\,(2n+1)\,\theta \tag{4.34}$$

where u_r, u_θ are the radial and circumferential components of non-dimensional flow velocity for a single cell, respectively, and $\eta = (r-1)/(1/\alpha)$. The coefficient A_n in Eqs. (4.32, 4.33, and 4.34) is:

$$\begin{aligned} A_n &\cong A_0 \left(\tfrac{a}{L}\right)^{2n+2} \left[-S_{2n+2} + (2n+3)\,(n+1)\,S_{2n+4} S_4 \left(\tfrac{a}{L}\right)^6 \right] \\ S_n &= 2^{-n} \sum_{k,\,m \neq 0} (k+im)^{-n} \qquad (k, m; \quad \text{integer}) \end{aligned} \tag{4.35}$$

where L is center-to-center distance of neighboring SMCs. Omitting the mathematical details, the effect of the volume fraction of a square array of SMCs, F, on the average WSS on a SMC is obtained using the analytical solutions Eqs. (4.32, 4.33, 4.34, and 4.35) as

$$\begin{aligned} \overline{\tau}^* &= \frac{\overline{\tau}}{\sqrt{U_0 \mu (-\Delta P/\Delta L)}} \\ &= \frac{4}{\pi} \frac{1 - 0.319285F^2 - 0.043690F^4}{\sqrt{\left(1 - F - 0.305828F^4\right)\left(1 + F - 0.305828F^4\right)}} \end{aligned} \tag{4.36}$$

where * represents the value is non-dimensional, ΔP is the pressure drop across the media, and ΔL is the thickness of the media. Equation (4.36) indicates that the WSS on an SMC is of the order $[U_0 \mu (-\Delta P/\Delta L)]^{1/2}$. To estimate the magnitude of the

WSS imposed by interstitial flow on SMCs, two sets of experimental data (Tedgui and Lever 1984) in rabbit thoracic aortas at 70 and 180 mmHg: (70 mmHg) $\mu = 1.0 \times 10^{-3}$ Pa s, $U_0 = 2.8 \times 10^{-6}$ cm/s, $-\Delta P = 52$ mmHg, $\Delta L = 125 \times 10^{-4}$ cm; and (180 mmHg) $\mu = 1.0 \times 10^{-3}$ Pa s, $U_0 = 4.39 \times 10^{-6}$ cm/s, $-\Delta P = 152$ mmHg, $\Delta L = 100 \times 10^{-4}$ cm were used. Notice that the pressure drop across the media is lower than the imposed pressure due to the resistance of the EC layer to the interstitial flow. The calculated average values of WSS were 0.55 dyn/cm^2 (70 mmHg) and 1.26 dyn/cm^2 (180 mmHg) when $F = 0.4$. The maximum values are about twice these values. On the other hand, mean values of WSS on ECs are on the order of 10 dyn/cm^2 in arteries and may be higher in capillaries and lower in postcapillary venules (Lipowsky 1995). The level of the WSS predicted in the present analysis was found to be similar to that on ECs, which can affect SMC biology (Shi and Tarbell 2011; Shi et al. 2009).

4.4.2.2 Numerical Computation of the Flow in Artery Wall

As seen in the previous subsection 4.4.2.1, SMCs could be subjected to significant levels of WSS associated with interstitial flow, even though the velocity of interstitial flow is very low (on the order of 10^{-6} cm/s). In this analytic model, the assumption of uniform flow velocity at the upstream end of an array of cylindrical SMCs neglected the more complex entrance conditions that exist at the intima-media boundary (Fig. 4.13). However, for the SMCs bordering the intima, the presence of IEL with leaky fenestral pores can greatly alter the flow field. Because the area fraction of fenestral pores is in the range 0.002–0.01 and the mean diameter of the fenestral pores varies from 0.4 to 2.1 μm (Huang et al. 1998), the velocity of fluid issuing from an individual pore could be 100-fold greater than the interstitial flow velocity in the media, resulting in a significant change in the distribution of

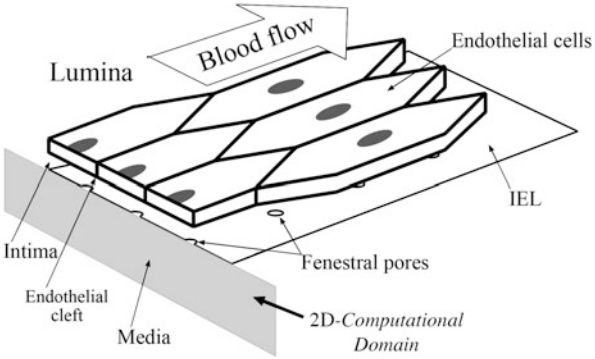

Fig. 4.13 Schematic illustration of the model for numerical simulation of interstitial flow in the media. The IEL separates the intima from the media and provides a complex entrance flow condition through the fenestral pores. The media consists of a periodic array of cylindrical SMCs embedded in a continuous, porous interstitial phase. Interstitial flow is distributed into the media from the intima through the fenestral pores in the IEL

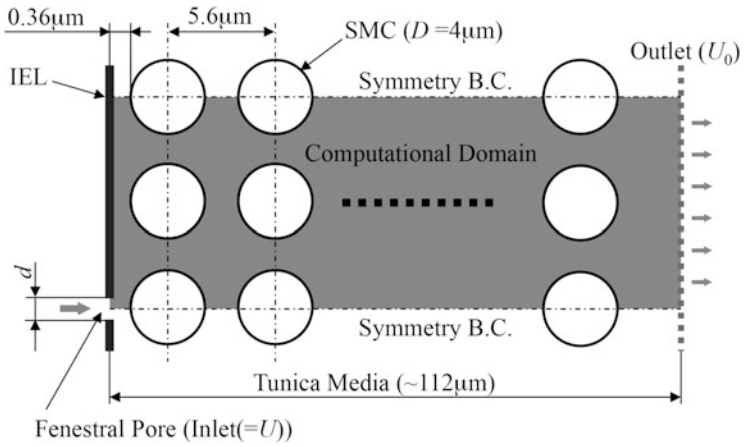

Fig. 4.14 Two-dimensional model of interstitial flow in the media (Modified from Tada and Tarbell 2000)

flow and associated WSS on the most superficial layer of SMCs that lie right beneath the IEL.

The geometry of the two-dimensional flow problem is shown in Fig. 4.14. The fenestral pore center is aligned with the SMC center to investigate the extreme case in which the WSS on SMCs attains the maximum possible value. SMCs are arranged in a square array configuration. To simplify the problem, the following assumptions are invoked: (1) The IEL is a rigid impermeable wall with zero thickness except for its fenestral openings. (2) The circular fenestral pores are distributed with a periodic square array configuration over the IEL surface. (3) The no-slip condition is applied on all surfaces of the SMCs and IEL. (4) A uniform velocity profile is specified at the entrance to the fenestral pores.

Once the SMC diameter, D ($=2a$), and volume fraction for SMC, F, are given, the distance between centers of neighboring SMCs, L, can be calculated. In the same manner, the pore spacing is also calculated when the pore diameter, d, and area fraction of pores, f, are given. The distance between the IEL and upstream end of the SMC, a, is taken as $a = 0.36$ μm in accordance with experimental data. All the physical constants and parameters used are listed in Table 4.2.

For the numerical simulations, FIDAP software package (version 7.62, FLUENT) was used. The set of governing equations, Eq. (4.31), was solved by direct Gaussian elimination. The finite element mesh realizations used in the numerical analysis is shown in Fig. 4.15. A symmetry boundary condition was applied on the top and bottom end lines of the computational domain. At the downstream end, a gradient-free ($dU/dx = 0$) outlet boundary condition was applied. In the vicinity of solid boundaries, a finer mesh of grid points taken perpendicular to each SMC surface was employed to ensure sufficiently high resolution within the boundary layer. The mesh size used was ~75,000.

Figure 4.16 shows streamlines of the interstitial flow in the media. The fluid coming from the fenestral pore is distributed into the whole region of the media. Near

Table 4.2 Physical constants and parameters used in numerical simulations

Parameter	Value
a [μm]	0.36
D [μm]	4.0
d [μm]	0.4–3.2
F	0.4
f	0.004, 0.016
K_p [cm^2]	1.43×10^{-14}
U_0 [cm/s]	5.80×10^{-6}
μ [Pa s]	6.86×10^{-3}
ρ [g/cm^3]	1.0

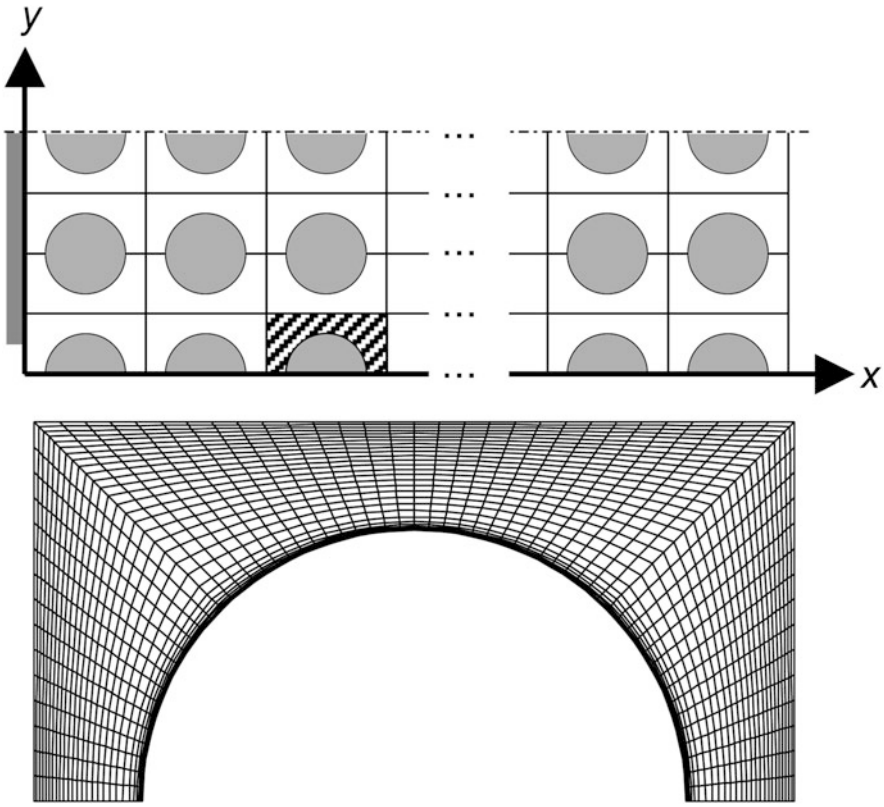

Fig. 4.15 The finite element mesh and the mesh configuration used in the numerical simulations (Reproduced from Tada and Ozono 2011 with permission from Springer)

the IEL, fluid spreads laterally into the upstream region as soon as it enters from the fenestral pore. At the narrowest point in the path between neighboring SMCs, the intervals between streamlines are almost equal, suggesting that a uniform velocity distribution is established except in a thin boundary layer near the SMC surfaces.

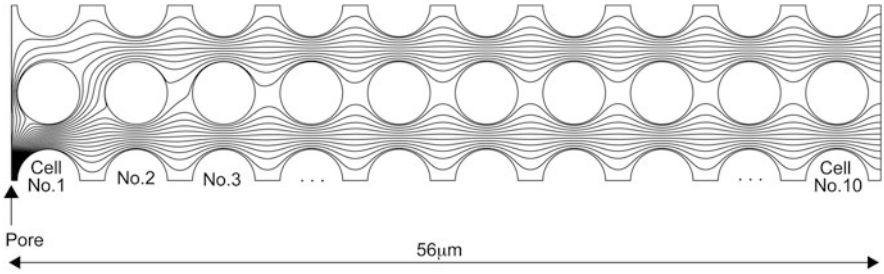

Fig. 4.16 A set of streamlines of the interstitial flow in the media. The figure is depicted only for the first 10 lines of the SMC array from the IEL (the *left end*) to show details of flow at the fenestral pore

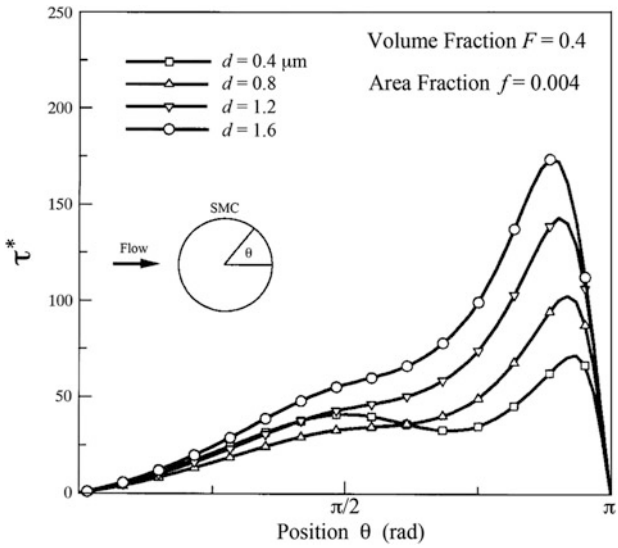

Fig. 4.17 Distributions of non-dimensional local shear stress along the circumference of the SMC right beneath a fenestral pore for four different values of fenestral pore diameter, d. The volume fraction of the SMC, F, and the area fraction of the fenestral pore, f, are kept constant at 0.4 and 0.004, respectively (Modified from Tada and Tarbell 2000)

This feature is quite different from conventional Stokes flow, in which the fluid displays a parabolic velocity distribution. Furthermore, streamlines penetrate more deeply into the wake region behind each SMC in contrast to those of Stokes flow.

Figure 4.17 shows the distribution of the non-dimensional local shear stress:

$$\tau^* \left(= \frac{\tau}{\sqrt{U_0 \mu (-\Delta p / \Delta L)}} \right) = -\mu \left[r \frac{\partial}{\partial r} \left(\frac{u_\theta}{r} \right) + \frac{1}{r} \frac{\partial u_r}{\partial \theta} \right] \Bigg|_{r=1} \tag{4.36}$$

along the circumference of the SMC right beneath a fenestral pore for four different values of fenestral pore diameter, d. F and f are kept constant at 0.4 and 0.004, respectively (Tada and Tarbell 2000).

To obtain a sense of the dimensional magnitude of these shear stresses, the normalization factor, $[U_0\mu(-\Delta P/\Delta L)]^{1/2}$, takes on a value of 0.52 dyn/cm^2 on the basis of interstitial flow data in the rabbit thoracic aorta (Tedgui and Lever 1984). Predictions show a significant elevation of shear stress on the first SMC. A constant value of f implies that the incoming flow velocity at the pore entrance is constant, independent of d.

4.4.3 Hemodynamics in Diseased Site of Artery Wall

The progression of intimal hyperplasia (IH) is affected by hemodynamic conditions at the diseased site of an artery wall, where SMCs are likely to migrate toward the sub-endothelial layer. A recent study showed that arterial levels of WSS act to suppress SMC migration by up-regulating the cellular production of NO, which in turn inhibits matrix metalloproteinase-2 (MMP-2) activity. It has been also shown in balloon catheter injury animal models (Tada and Tarbell 2000) where superficial layers of SMC are exposed directly to blood flow that intimal thickening in the absence of the endothelium is accelerated in low WSS environments, suggesting that SMCs exposed to blood flow respond directly to changes in blood flow. However, other recent studies have shown that even in the case of an intact endothelium, SMCs are subjected to WSS through exposure to interstitial flow driven by the transmural pressure gradient (Wang and Tarbell 1995; Tada and Tarbell 2000, 2002).

Shi et al. (2011) showed experimentally in a 3D collagen gel model of suspended SMC exposed to interstitial flow that increased interstitial flow, such as that which occurs at sites of elevated EC hydraulic conductivity in vascular disease, leads to an enhancement SMC migration that could contribute to enhanced IT. They also demonstrated the role of the surface layer of proteoglycans bound to the SMC (the glycocalyx) in mediating the mechanotransuction of interstitial flow shear stress by the SMC. The glycocalyx represents the additional thin matrix layer (order 1 μm thick) on the cell surface that is involved in transmitting fluid shear stress to the cell surface through the solid core proteins of the bound proteoglycan molecules in the surface glycocalyx layer. In a related theoretical study, Tarbell and Shi (2013) deduced that the solid shear stress component transmitted to the cell could be 10 times the imposed fluid shear stress on the surface of the glycocalyx. This suggests WSS values of 5–10 dyn/cm^2 on SMC surface imposed by interstitial flow. These stresses are essentially the same as imposed by blood flow on EC.

Although the biological evidence is still limited at the present time, it is reasonable to speculate that interstitial flow affects the function of SMCs in addition to their migration. While in the realm of speculation, it should also be noted that

alterations in blood pressure and endothelial hydraulic conductivity will affect interstitial flow and in turn the WSS on SMCs. The above issues have been extensively reviewed by Shi and Tarbell (2011).

References

Ajmani RS (1997) Hypertension and hemorheology. Clin Hemorheol Microcirc 17:397–420

Bor-Kucukkatay M, Yalcin O, Gokalp O et al (2000) Red blood cell rheological alterations in hypertension induced by chronic inhibition of nitric oxide synthesis in rats. Clin Hemorheol Microcirc 22:267–275

Chien S (2003) Molecular mechanical bases of focal lipid accumulation in arterial wall. Prog Biophys Mol Biol 83:131–151

Chien S, Dormandy J et al (eds) (1987) Clinical hemorheology. Martinus Nijhoff Publishers, Dordrecht

Clark JM, Glagov S (1985) Transmural organization of the arterial media: the lamellar unit revisited. Arterioscler Thromb Vasc Biol 5:19–34. doi:10.1161/01.ATV.5.1.19

Fung YC (1993) Biomechanics: mechanical properties of living tissues, 2nd edn. Springer, New York

Huang Y, Jan KM, Rumschitzki D et al (1998) Structural changes in rat aortic intima due to transmural pressure. Trans ASME J Biomech Eng 120:476–483

Kesmarky G, Toth K, Habon L et al (1998) Hemorheological parameters in coronary artery disease. Clin Hemorheol Microcirc 18:245–251

Kleinstreuer C (2006) Biofluid dynamics: principles and selected applications. CRC Press, Boca Raton

Kohler TR, Jawien A (1992) Flow affects development of intimal hyperplasia after arterial injury in rats. Arterioscler Thromb 12:963–971

Ku DN, Giddens DP et al (1985) Pulsatile flow and atherosclerosis in the human carotid bifurcation: positive correlation between plaque location and low oscillating shear stress. Arteriosclerosis 5:293–302

Levick JR (1987) Relation between hydraulic resistance and composition of the interstitium. Adv Microcirc 13:124–133

Lipowsky HH (1995) Shear stress in the circulation. In: Bevan JA et al (eds) Flow-dependent regulation of vascular function. Oxford University Press, New York

McMillan DE (1993) Hemorheological studies in the diabetes control and complications trial. Clin Hemorheol 13:147–154

Merrill EW (1969) Rheology of blood. Physiol Rev 49(4):863–888

Morris CL, Rucknagel DL et al (1989) Evaluation of the yield stress of normal blood as a function of fibrinogen concentration and hematocrit. Microvasc Res 37(3):323–338

Ramakrishnan S, Grebe R et al (1999) Aggregation of shape altered erythrocytes: an in vitro study. Curr Sci 77:805–808

Shi ZD, Tarbell JM (2011) Fluid flow mechanotransduction in vascular smooth muscle cells and fibroblasts. Ann Biomed Eng 39(6):1608–1619

Shi ZD, Ji XY, Qazi H et al (2009) Interstitial flow promotes vascular fibroblast, myofibroblast, and smooth muscle cell motility in 3-D collagen I via upregulation of MMP-1. Am J Physiol Heart Circ Physiol 297(4):H1225–H1234

Shi ZD, Wang H et al (2011) Heparan sulfate proteoglycans mediate interstitial flow mechanotransduction regulating MMP-13 expression and cell motility via FAK-ERK in 3D collagen. PLos One. doi:10.1371/journal.pone.0015956

Shul'man ZP, Mansurov VA et al (2006) Rheological changes in the blood and plasma of patients with myocardial ischemia and diabetes mellitus and dysfunction of their endothelium. J Eng Phys Thermophys 79(1):99–104

Tada S, Ozono H (2011) Computational study of LDL mass transport in the artery wall. J Biorheol 25(1–2):27–35

Tada S, Tarbell JM (2000) Interstitial flow through the internal elastic lamina affects shear stress on arterial smooth muscle cells. Am J Physiol Heart Circ Physiol 278:H1589–H1597

Tada S, Tarbell JM (2002) Flow through internal elastic lamina affects shear stress on smooth muscle cells (3D simulations). Am J Physiol Heart Circ Physiol 282:H576–H584

Tada S, Tarbell JM (2005) A computational study of flow in a compliant carotid bifurcation – stress phase angle correlation with shear stress. Ann Biomed Eng 33:1202–1212

Tarbell JM, Shi ZD (2013) Effect of the glycocalyx layer on transmission of interstitial flow shear stress to embedded cells. Biomech Model Mechanobiol 12(1):111–121. doi:10.1007/s10237-012-0385-8

Tarbell JM, Shi ZD et al (2014) Fluid mechanics, arterial disease, and gene expression. Annu Rev Fluid Mech 46:591–614. doi:10.1146/annurev-fluid-010313-141309

Tedgui A, Lever MJ (1984) Filtration through damaged and undamaged rabbit thoracic aorta. Am J Physiol Heart Circ Physiol 247:H784–H791

Thomas JB, Milner JS et al (2002) On the influence of vessel planarity on local hemodynamics at the human carotid bifurcation. Biorheology 39:443–448

Wang DM, Tarbell JM (1995) Modeling interstitial flow in an artery wall allows estimation of wall shear stress on smooth muscle cells. Trans ASME J Biomech Eng 117:358–363